JCTA Journal of Computing Theories and Applications ISSN:3024-9104

Research Article

Exhaustive Entanglement-Topology Enumeration and Edge-Vertex-Level Attribution in Quantum Feature Map Design for Classification

Natanael, Hendrik Sugiarto *, and Yozef Tjandra

Department of Information Technology and Big Data Analytics, Calvin Institute of Technology, Jakarta 10610, Indonesia;
e-mail : natanael@calvin.ac.id; hendrik.sugiarto@calvin.ac.id; yozef.tjandra@calvin.ac.id
* Corresponding Author : Hendrik Sugiarto

Abstract: Quantum kernel methods encode classical data into quantum states using specially designed feature-map circuits and then train a classical SVM on the resulting kernel matrix. Prior studies of entanglement structure typically compare only a few basic topologies, such as linear, circular, and full entanglement, leaving the broader space of entanglement graphs largely unexplored. This study exhaustively evaluates all possible entanglement topologies of a TwoLocal feature map and benchmarks them against classical methods and standard quantum feature maps on two synthetic datasets (Adhoc3_150 and Adhoc4_150) and two real-world datasets (Blood and Banknote). On Adhoc4_150, the best TwoLocal topology achieves an accuracy of 0.7556, matching Pauli Z; on Blood, it reaches 0.6889, exceeding RBF SVM and Pauli Z at 0.6667; and on Banknote, it achieves 1.0000, compared with 0.9778 for RBF SVM. In contrast, Random Forest achieves the highest accuracy on Adhoc3_150 at 0.8222, exceeding all evaluated quantum configurations. Across all four datasets, increasing the number of entangling pairs does not consistently improve accuracy, while the standard linear, circular, and full Pauli ZZ topologies never outperform Pauli Z. To further characterize this behavior, we propose a factorial linear modeling approach that quantifies the contribution of individual entanglement edges and qubit connectivity to classification accuracy. On Adhoc4_150, two edges exhibit significant negative effects, whereas Blood and Banknote show both significant positive and negative edge effects. The q0q1 edge is significant across all three four-feature datasets but reverses direction across datasets. These results indicate that the effect of entanglement depends jointly on the feature-map architecture, dataset, and specific qubit connections rather than on entanglement density alone. The proposed framework can also be applied to sampled topology sets, providing a basis for targeted entanglement analysis beyond exhaustively enumerable low-qubit systems.

Keywords: Edge-Level Attribution; Entanglement Topology; Factorial Regression Analysis; Quantum Feature Map; Quantum Kernel Method; Quantum Machine Learning; Quantum Support Vector Machine (QSVM); TwoLocal Ansatz.

Received: July, 6th 2026
Revised: August, 12th 2026
Accepted: August, 17th 2026
Published: September, 11th 2026

1. Introduction

Quantum computing has been recognized as a potentially revolutionary computational paradigm, promising to solve intractable problems that remain challenging for classical computers. The scheme is uniquely identified by the exploitation of quantum physical phenomena such as superposition, entanglement, and interference [1]. While large-scale, fault-tolerant quantum advantage is still an open engineering challenge, current noisy intermediate scale quantum (NISQ) devices [2] and quantum simulators have already enabled meaningful experimentation across several domains, including chemistry simulation [3], optimization , and cryptography [4]. Among these, the field of machine learning has emerged as one of the most actively explored application areas [5], motivated by the idea that quantum-mechanical feature

spaces may offer representational or computational advantages over purely classical models for certain data structures.

This intersection, commonly referred to as quantum machine learning (QML), spans several distinct approaches rather than a single method. Variational quantum circuits (VQCs) parameterize a quantum circuit and optimize its parameters using a classical-quantum hybrid training loop, and have been applied to tasks ranging from complex-valued data classification [6] to accelerator physics [7]. Quantum neural networks (QNNs) [8] and quantum convolutional neural networks (QCNNs) [9] adapt neural network style architectures to quantum circuits, and have been used in distributed and federated settings, including federated QCNNs trained across edge devices and quantum tensor networks applied to large-scale medical imaging datasets [10].

A particular approach on which this study is built, is the quantum kernel method, where a fixed (non-trained) feature-map circuit encodes classical data into quantum states, and a classical kernel-based classifier, typically a Support Vector Machine (SVM), is trained on the resulting quantum kernel matrix. Quantum kernel methods were first formalized by Havlíček et al. [11], who proposed and experimentally implemented two quantum algorithms that use quantum state space as a feature space. The work argues that a quantum-enhanced feature space efficiently accessible only on a quantum computer might offer a possible path to quantum advantage. Their construction, and the associated ad hoc dataset generation procedure now bundled with IBM Qiskit [12], [13], remains the standard reference point for quantum kernel SVM (QSVM) experimentation. Subsequent theoretical work by [14] examined why entanglement structure matters for feature map design, showing that it directly shapes how well a quantum circuit's performance can be characterized and controlled. Investigating quantum kernels specifically is motivated by this Hilbert-space argument: since entanglement structure is a design choice with no direct classical counterpart, understanding how it shapes the induced kernel is an essential task. In fact, it serves as a prerequisite for evaluating quantum kernel methods on their own terms, independent of whether a given quantum kernel ultimately outperforms a classical alternative on a specific dataset.

Within the quantum kernel method, the entanglement structure of the feature map is one of the most important architectural choices since it shapes how the resulting kernel embeds classical data into the Hilbert space and how well different classes separate under it [14]. A growing body of work has tested how varying this entanglement structure affects quantum kernel SVM accuracy. However, this literature consistently restricts its comparisons to a fixed set of basic topologies such as the 'linear', 'full', or 'circular' schemes; instead of exhaustively analyze the space of all possible entanglement graphs. This restriction carries a direct scientific cost, not just a coverage gap. Basic topologies differ in both edge count and edge identity at once, so any accuracy difference between them could stem from either factor of which the two are confounded and cannot be told apart. As a result, existing comparisons cannot establish whether a topology's effect on accuracy comes from entanglement density in general or from the specific qubit pairs it happens to connect. This is a distinction which is directly actionable for feature map design, since it determines whether a practitioner should add entanglement indiscriminately or target specific qubit pairs. For a small number of qubits, this space is still practically enumerable, yet no existing study evaluates this space exhaustively.

In this work, we exploit the tractable size of the entanglement-graph space in the low-qubit setting to exhaustively capture how entanglement topology in quantum feature maps affects classification accuracy. In addition, we employ a factorial linear modeling framework to statistically quantify the effects of entanglement elements (both edges and qubit degree) on classification accuracy, moving beyond simple aggregate comparisons to capture the sensitivity of classification accuracy to individual entanglement elements.

Structurally, this statistical framework is not limited to the low qubit, exhaustive enumeration setting studied here. Since the factorial model only requires a set of topologies and their corresponding accuracy values as input, its formulation is not mathematically restricted to exhaustive enumeration. In principle, the same model could be fit on a representative sample of entanglement topologies at higher qubit counts, where exhaustive enumeration becomes computationally infeasible. We note, however, that the qubit-scalable character of the framework described here is a property of its mathematical formulation, not a demonstrated empirical result. What we claim transfers beyond the low qubit systems studied here is the attribution technique itself, not the specific coefficients reported for these datasets. The contribution of this work is threefold:

1. An empirical comparison of classical non-kernel method (Random Forest and Gradient Boosting), classical kernel SVM (linear, polynomial, and RBF), against quantum kernel SVM using standard (Z and ZZ feature maps) and TwoLocal feature maps.
2. An exhaustive evaluation of classification performance against all possible entanglement graph topologies in TwoLocal feature maps, particularly for the three and four qubit systems evaluated in this study.
3. A statistical analysis approach, based on factorial linear regression, that decomposes the marginal contribution of individual entanglement edges and qubit degrees to classification accuracy within the enumerated topology space evaluated.

The remaining sections of this article are organized as follows. Section 2 reviews related work on quantum kernel methods and entanglement structure in feature maps. Section 3 describes the proposed method, including dataset preparation, feature map implementation, and the experimental setup. Section 4 presents the experimental results, statistical analysis, and discussion. Finally, Section 5 summarizes and concludes the paper.

2. Related Works

2.1. Quantum Kernel Method and Quantum Feature Map

Support Vector Machine (SVM) is a popular classification machine learning model whose goal is to discover an optimal hyperplane that serves as the best decision boundary separating data points with different labels [15]. However, real data are often inseparable simply by a linear hyperplane. To overcome this, ones could apply the kernel trick [16], where the original data points are mapped into higher dimensional space so that a linear hyperplane would be able to separate interclass data. In practice, RBF (radial-based function) [17] is one among many commonly used kernels for performing the trick.

A quantum kernel replaces the classical similarity function with one computed on a quantum computer. Classical data $\vec{x}$ is encoded into a quantum state $|\varphi(\vec{x})\rangle$ through a parameterized quantum circuit known as a feature map. Next, the kernel value is defined as the squared overlap between two encoded states:

$$K\left(\vec{x}, \vec{x'}\right) = |\langle\varphi(\vec{x})|\varphi\left(\vec{x'}\right)\rangle|^2 \quad (1)$$

Since this overlap is evaluated in a Hilbert space whose dimension grows exponentially with the number of qubits, quantum feature maps can in principle represent similarity structures that are difficult to reproduce classically [11]. The structure of the feature map circuit, including the arrangement of entangling gates between qubits, significantly determines the geometry of this induced feature space, which contributes directly to the classification results [18]. Figure 1 provides a high-level illustration of how classical and quantum kernels are employed to enhance an SVM classification.

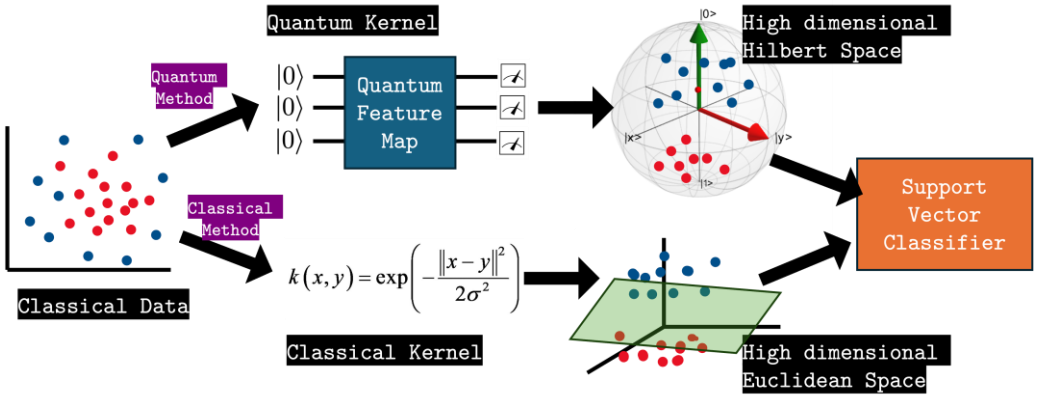

Figure 1. Quantum and Classical Kernels for SVM Classification

In practice, the quantum kernel matrix is initially computed once in a quantum fashion, and is then passed as a precomputed kernel to a standard classical SVM solver. No other

component of the SVM algorithm is modified, meaning that only the kernel matrix differs between the classical and quantum conditions evaluated in this paper.

2.2. Entanglement in Quantum Feature Maps

Entanglement is widely regarded as a fundamental resource in quantum information processing, with applications ranging from quantum communication to quantum computation [1], [2]. In quantum machine learning, its role has been studied through the related concepts of expressibility and entangling capability introduced in [14]. Expressibility measures the extent to which a feature map generates diverse quantum states across the Hilbert space as the input varies, whereas entangling capability measures the tendency of the circuit to generate entangled rather than separable states. Both properties provide circuit-level measures for characterizing how the design of a feature map may influence downstream performance. However, they summarize the behavior of an entire circuit into aggregate quantities and do not identify the contribution of individual entanglement edges or qubit connectivity patterns.

Several empirical studies have investigated the relationship between entanglement structure and QSVM performance by comparing different feature-map topologies. Comparisons between linear and fully entangled circuits have generally favored full entanglement, with [19] reporting higher performance for fully entangled circuits across most evaluated features. Other work has extended this comparison to circular entanglement [20], considering linear, circular, and full entanglement as distinct circuit structures and, consequently, distinct quantum kernels. The magnitude and direction of the observed benefit, however, vary across datasets. For example, [21] reported a 45% accuracy improvement for an entanglement-enhanced kernel on a complex respiratory dataset, while performance was comparable to classical methods on simpler and more linearly structured data. In contrast, [22] found that a ZZFeatureMap-based kernel did not outperform a classical Gaussian kernel at four qubits. Entangled-state initialization strategies have also been reported to improve classification accuracy by up to 10% on selected benchmark datasets when compared with separable-state initialization [23]. More recently, [24], [25] employed metaheuristic optimization to search for entanglement configurations together with the kernel classification procedure, suggesting that suitable entanglement structures may be dataset dependent.

Collectively, these studies indicate that entanglement can influence quantum-kernel classification performance, but they primarily treat the feature-map topology as a single design unit. Comparisons between linear, circular, and full entanglement simultaneously modify multiple edges and qubit connectivity degrees, making it difficult to determine which structural elements are responsible for an observed performance change. Similarly, metaheuristic optimization identifies high-performing configurations but does not characterize the contribution of individual edges or the broader topology space, particularly for configurations that are not selected during the search. Consequently, the existing evidence establishes that entanglement structure matters, but provides limited information about how individual connectivity choices contribute to classification performance.

A further limitation concerns the completeness of topology evaluation. Existing comparisons generally consider a small set of predefined topologies or a selected configuration produced through optimization rather than systematically evaluating all feasible connectivity patterns. As a result, conclusions about the relative benefit of a particular entanglement pattern remain dependent on the candidate structures included in the experiment. This motivates a more systematic examination of the topology space in which individual edge configurations can be evaluated under a common feature-map architecture.

2.3. Prior Work on Entanglement and Attribution in Quantum Kernel Methods

Recent large-scale benchmarking studies provide an important complementary perspective by questioning whether entanglement is consistently beneficial for quantum kernel methods. Bowles et al. [26] evaluated several quantum machine learning models, including quantum neural networks, fidelity quantum kernels, and projected quantum kernels, across multiple datasets and reported that data-encoding circuits without entanglement can perform competitively. This finding challenges the assumption that entanglement is inherently necessary for achieving improved quantum-kernel performance. Schnabel and Roth [27] extended this analysis through a large-scale benchmark comprising more than 20,000 trained quantum kernel models across five dataset families, 64 datasets, nine data-encoding circuits, and both

fidelity and projected quantum kernels. Their results similarly showed that non-entangled circuits often performed on par with or better than their entangled counterparts. Their hyperparameter analyses further indicated that regularization strength and feature scaling generally had a stronger influence on performance than the number of qubits or circuit layers for the datasets considered.

These studies establish an important aggregate-level finding: the presence of entanglement alone does not reliably explain quantum kernel performance. However, aggregate benchmarking does not reveal whether the observed variability originates from particular entanglement edges or qubit connectivity patterns within a feature map. Understanding this structural level of variation requires an attribution mechanism capable of distinguishing the contribution of individual circuit components.

Gate-level attribution has recently been explored through quantum-circuit explainability methods. Heese et al. [28] proposed Shapley values for quantum circuit explanations (SVQXs), treating individual gates as players in a coalition game and assigning attribution scores with respect to value functions such as classification accuracy, expressibility, and entangling capability. Because exact Shapley-value computation requires evaluating all coalitions of active gates, the method employs sampling-based estimators for circuits with a nontrivial number of gates. The framework was demonstrated in several applications, including a QSVM feature map in which individual gates, including entangling CX gates, were attributed with respect to test accuracy. The results showed that individual entangling gates can have negligible or even negative contributions to classification performance, providing a gate-level perspective consistent with the broader entanglement-agnostic findings reported in [26] and [27].

The existing literature therefore provides two complementary perspectives. Large-scale benchmarking demonstrates that entanglement is not consistently associated with improved quantum-kernel performance [26] and [27], while gate-level attribution demonstrates that individual circuit components can contribute differently to a model's performance [28] Neither perspective, however, directly characterizes the contribution of individual entanglement edges across the feasible topology space of a common feature-map architecture. The former evaluates entanglement primarily as an aggregate circuit property, whereas the latter attributes arbitrary gates within selected circuits and relies on sampling when the number of gates increases.

The present study addresses this intermediate structural level by exhaustively enumerating feasible entanglement subsets within a fixed TwoLocal feature-map architecture and modeling their resulting classification accuracies using factorial linear models with effect coding. This design enables exact edge-level and qubit-level attribution within the evaluated topology space, rather than identifying only a single high-performing topology or attributing effects to individual gates in an already selected circuit. The resulting analysis distinguishes whether performance variation is associated with the presence of specific entanglement edges, qubit connectivity, or overall entanglement density, thereby providing a more granular structural account of the role of entanglement in quantum kernel classification.

3. Proposed Method

This work proposes an evaluative framework to investigate how different entanglement schemes affect the classification performance of quantum feature maps in a quantum kernel SVM. As illustrated in Figure 2, the framework follows a unified pipeline. First, the classification datasets are prepared through the preprocessing procedure described in Section 3.1. The resulting feature vectors are then encoded into quantum states using the feature maps considered in this study, including an exhaustively generated set of entanglement topologies for the TwoLocal circuit. For each configuration, a quantum kernel matrix is computed and provided to a classical SVM to obtain the corresponding classification performance. The accuracy values obtained across the exhaustively enumerated TwoLocal topologies are subsequently used as inputs to the factorial linear models described in Section 4.2. These models quantify the sensitivity of classification performance to individual entanglement edges and qubit connectivity.

The complete pipeline therefore consists of data preprocessing, quantum feature-map construction, quantum kernel computation, QSVM classification, and structural sensitivity analysis. This consistent procedure enables the effects of different entanglement

configurations to be evaluated under the same experimental conditions and provides a basis for relating topology-level performance differences to individual edge and qubit-level effects.

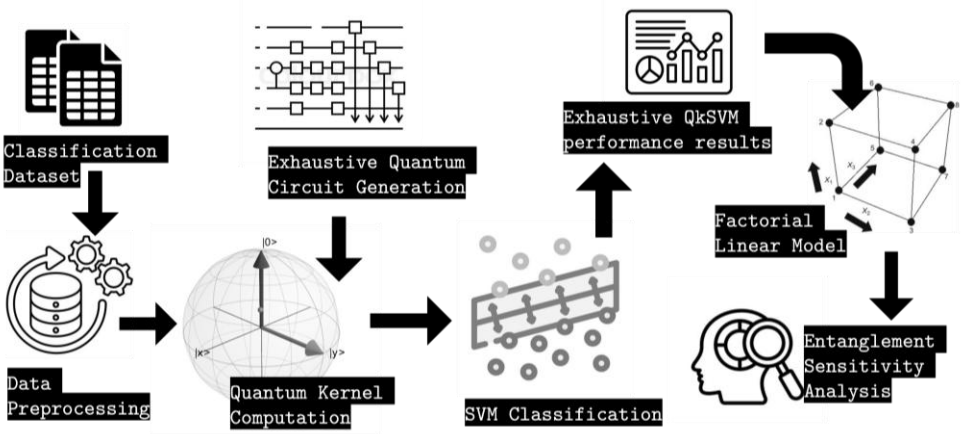

Figure 2. Pipeline Overview of the Proposed Quantum Kernel SVM Entanglement Evaluative Framework

3.1. Data Preprocessing

The synthetic datasets used in this study belong to the multidimensional Adhoc dataset family introduced in [11]. Specifically, datasets with dimensionality $n \in \{3,4\}$ and 150 observations were generated, with balanced class distributions. These datasets are referred to as Adhoc3_150 and Adhoc4_150, respectively. Each feature value x_i was randomly sampled from a uniform distribution over $[0,\ 2\pi)$, and the class label (y) was determined by the sign of the product of sinusoidal transformations across all feature components:

$$y = \text{sign}\left(\prod_{i=1}^{n} \sin(x_i)\right). \tag{2}$$

This labeling scheme produces highly nonlinear decision boundaries, making the Adhoc dataset family well-suited as a benchmark for evaluating the ability of quantum kernels to capture complex data structures that are difficult to separate with simple linear models.

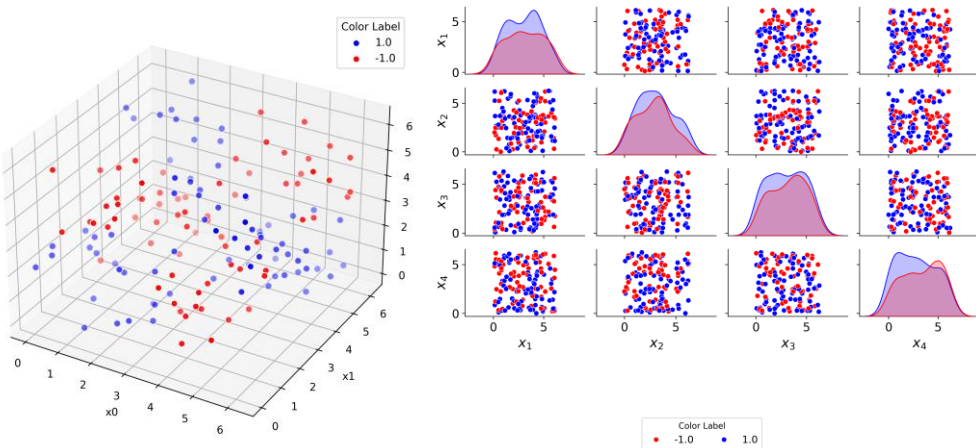

Figure 3. Visualisation of Adhoc Dataset with 3 features (left); and 4 features (right)

The distributional characteristics of the synthetic datasets with 3 and 4 features are visualized in Figure 3. The two classes (labels 1.0 and -1.0) substantially overlap across the feature space without forming clearly linearly separable clusters, while their marginal distributions are also highly similar. This distribution is consistent with the nonlinear labeling function used to generate the datasets.

The Adhoc dataset family used in this study was designed to maintain an approximately balanced class distribution. Before quantum encoding, each dataset was partitioned into training and testing sets. The raw feature vectors (x_{raw}) were then normalized to the interval [-1, 1], using MinMaxScaler, with the scaling parameters fitted exclusively on the training set and subsequently applied to the test set. This procedure prevents information from the test distribution from influencing preprocessing and ensures a valid model evaluation. Bounded feature values also help control the input range of angle-based quantum encodings and mitigate excessive rotation effects associated with the 2π-periodicity of quantum rotation gates, preventing data redundancy, and improving the numerical stability of angle-based encoding schemes [29]. Specifically, the normalization process is defined as:

$$x = 2\left(\frac{x_{\text{raw}} - x_{\text{min}}}{x_{\text{max}} - x_{\text{min}}}\right) - 1 \tag{3}$$

where x_{min} and x_{max} are the minimum and maximum values computed solely from the training data and subsequently reused to scale the test data.

To complement the synthetic datasets, the approach was also evaluated on two publicly available real-world datasets: the Blood Transfusion Service Center [30] and Banknote Authentication [31] dataset. Both datasets contain four numerical features and a binary target. Each dataset was undersampled to 150 instances with balanced class sizes to maintain practical computational requirements for quantum-kernel evaluation. The Blood dataset was selected because previous studies have reported it as a nontrivial classification problem for classical models [24], [25], particularly in the context of examining the contribution of entanglement to machine learning performance. The Banknote dataset was included to provide additional variability among the real-world datasets, representing a physical document forgery domain alongside the clinical context of the Blood dataset.

3.2. Quantum Feature Maps: Baselines and the Customized Entangled Scheme

This work compares the classification performance of quantum feature maps under exhaustive entanglement-topology enumeration with both classical and quantum baselines. Two categories of classical baselines are considered. The first consists of kernel-based methods, including linear, polynomial (degree 3), and RBF kernel SVMs [17], which are widely used in classical SVM practice. The second consists of non-kernel-based methods, namely Random Forest and Gradient Boosting [32], which are included as widely used ensemble learning approaches. The two categories serve different purposes. Kernel-based methods provide a direct comparison with quantum kernel methods because both operate within the SVM framework and differ primarily in how the kernel is computed. Non-kernel-based methods provide a broader reference for assessing the performance of the quantum approaches against conventional classification methods.

On the quantum side, two commonly used feature maps for quantum kernel SVM are considered. The ZFeatureMap provides a non-entangled first-order Pauli-Z encoding, whereas the ZZFeatureMap extends the encoding to second-order interactions through entangling gates between qubit pairs [11]. Figure 4 illustrates the ZFeatureMap circuit for the Adhoc3_150 dataset. Under the same qubit count, Figure 5 presents the ZZFeatureMap using linear, circular, and full entanglement schemes.

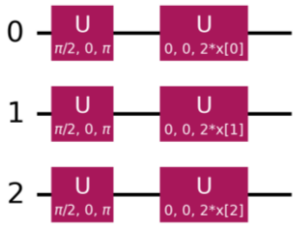

Figure 4. Pauli ZFeatureMap Circuit

To enable arbitrary variation of the entanglement structure across possible qubit connectivity patterns, the TwoLocal class from the Qiskit circuit library is used as the underlying circuit architecture. TwoLocal was originally designed as a parameterized ansatz for variational algorithms, typically with trainable weights optimized during training. In this study, it

is repurposed as a customizable feature map by binding its circuit parameters directly to the input data rather than using trainable weights.

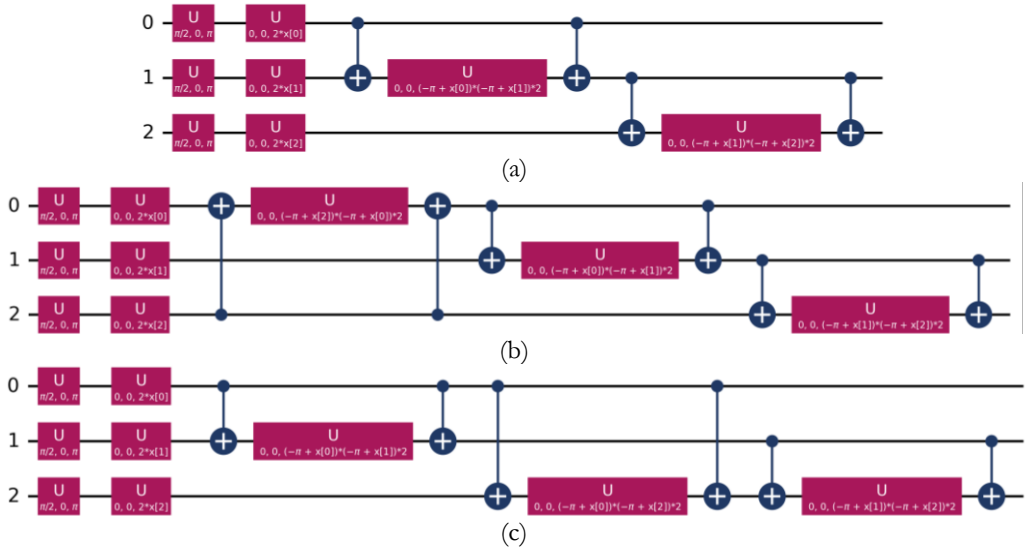

Figure 5. Pauli Z feature map circuits under different entanglement topologies: (**a**) linear; (**b**) circular; and (**c**) full entanglement

The TwoLocal circuit consists of alternating rotation and entanglement blocks. The rotation layer applies single-qubit gates to each qubit, while the entanglement layer applies two-qubit gates according to a specified connectivity pattern. These layers can be repeated according to the selected repetition parameter. The parameters used for the quantum feature maps are summarized in Table 1. Figure 6 presents representative TwoLocal feature maps with customized entanglement schemes for four data features. The illustrated connectivity patterns represent non-standard topologies that are not captured by the conventional linear, circular, or full schemes.

Table 1. Parameters Setup for The Studied Quantum Feature Maps.

Parameter	Pauli Z	Pauli ZZ	TwoLocal
reps	1	1	1
rotation_block	RZ	RZ	RX
entanglement_block	-	CZ	CX
entanglement_type	-	{linear, circular, full}	custom

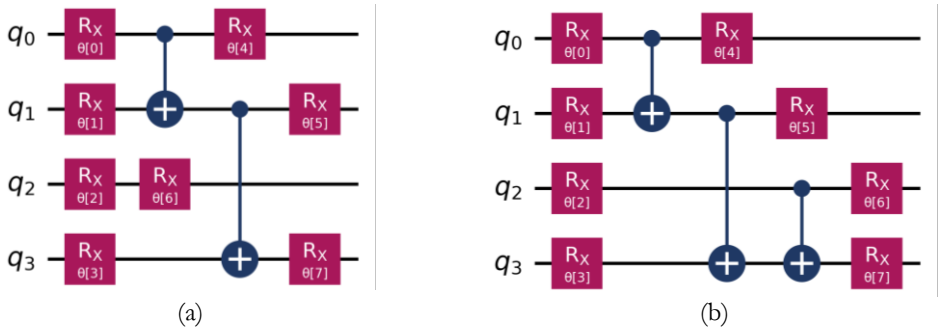

Figure 6. TwoLocal feature map circuits with different customized entanglement schemes: (**a**) RX Ansatz-{(0,1), (1,3)}; and (**b**) RX-Ansatz{(0,1), (1,3), (2,3)}

The classical baselines are not intended to demonstrate quantum superiority, as discussed in [33]. The dataset used in this comparison is generated in a manner that favors quantum-style feature interactions. Therefore, any performance difference in favor of the quantum methods should not be interpreted as evidence of quantum advantage. Demonstrating

quantum advantage is outside the scope of this work; the classical baselines are included to contextualize the quantum results within the broader classification landscape.

3.3. Classification Experimental Setup

All experiments were implemented in Python using Qiskit [12] for quantum circuit construction and simulation and Qiskit Machine Learning [13] for quantum kernel support vector classification. The quantum feature maps and corresponding kernels were evaluated using noiseless statevector simulation. Classical SVM models with conventional kernels were implemented using Scikit-learn [34]. The versions of the computational libraries are summarized in Table 2. The simulations were performed on a classical workstation equipped with an Intel Core i7-12700F CPU, 32 GB of system RAM, and an NVIDIA GeForce RTX 4080 GPU with 16 GB of VRAM, running Ubuntu 24.04.4 LTS. The hardware configuration is summarized in Table 3. GPU acceleration was used for the quantum simulation workloads.

Table 1. Computational Library Versions

Library	Version
Qiskit	1.0.2
Qiskit Aer (GPU)	0.14.1
Qiskit Machine Learning	0.7.2
Qiskit Algorithms	0.3.0
Scikit-learn	1.6.1

Table 2. Hardware Specification

Aspects	Value
CPU Model	Intel Core i7-12700F
System RAM	32 GB
Operating System	Ubuntu 24.04.4 LTS
GPU Model	NVIDIA GeForce RTX™ 4080
GPU VRAM	16 GB

The comparative evaluation uses classification accuracy as the primary performance metric. Since all datasets were constructed or sampled with balanced class sizes, accuracy provides a direct measure of the proportion of correctly classified instances and enables consistent comparison across the classical kernels, Pauli Z, Pauli ZZ, and TwoLocal configurations. Precision, recall, and F1-score are additionally reported in the experimental results to provide complementary performance measures. For each dataset, the preceding experimental procedure produces one classification result for each evaluated feature-map configuration, including every exhaustively enumerated TwoLocal entanglement topology. The resulting topology–accuracy observations constitute the response data for the factorial sensitivity analysis described in Section 4.2. Because the TwoLocal topology space is exhaustively evaluated within the considered qubit scale, the subsequent edge- and vertex-level models are fitted using the complete set of evaluated topologies rather than a manually selected or metaheuristically sampled subset [24], [25].

4. Results and Discussion

4.1. Quantum Feature Map Performance

This section presents the classification performance of the evaluated classical and quantum feature-map configurations across the four datasets. Table 4 reports accuracy, precision, recall, and F1-score for the classical baselines, Pauli Z, the three standard Pauli ZZ topologies, and the best-performing TwoLocal configuration for each dataset. For the TwoLocal feature map, the results are additionally grouped according to the number of entangling pairs, with the mean and standard deviation reported for each group. At the maximum number of entangling pairs, only one topology is possible for a given qubit count; therefore, no standard deviation is reported for these configurations.

Table 3. Classification Models evaluated using Various Evaluation Metrics Across Datasets

Dataset	Family	Model	Accuracy	Precision	Recall	F1
Adhoc3_150	Classical: NonKernel	Random Forest	0.8222	0.8000	0.8696	0.8333
		Gradient Boosting	0.5778	0.5769	0.6522	0.6122
	Classical: Kernel	Linear SVM	0.4889	0.5000	0.6522	0.5660
		Polynomial SVM	0.8000	0.7333	0.9565	0.8302
		RBF SVM	0.7778	0.7407	0.8696	0.8000
	Pauli Z	Pauli Z	0.7778	0.7407	0.8696	0.8000
	Pauli ZZ	Linear	0.4000	0.4167	0.4348	0.4255
		Circular	0.6222	0.6154	0.6957	0.6531
		Full	0.6222	0.6154	0.6957	0.6531
	TwoLocal	1-pair mean	0.7778±0.0000	0.7304±0.0179	0.8986±0.0502	0.8049±0.0086
		2-pair mean	0.7037±0.0642	0.6755±0.0565	0.8116±0.0502	0.7373±0.0543
		3-pair mean	0.6667	0.6429	0.7826	0.7059
	TwoLocal	Best: (0,1)	0.7778	0.7407	0.8696	0.8000
Adhoc4_150	Classical: NonKernel	Random Forest	0.5111	0.5556	0.6000	0.5769
		Gradient Boosting	0.5778	0.6154	0.6400	0.6275
	Classical: Kernel	Linear SVM	0.5556	0.5556	1.0000	0.7143
		Polynomial SVM	0.5778	0.5789	0.8800	0.6984
		RBF SVM	0.5556	0.5714	0.8000	0.6667
	Pauli Z	Pauli Z	0.7556	0.7917	0.7600	0.7755
	Pauli ZZ	Linear	0.5556	0.5806	0.7200	0.6429
		Circular	0.5556	0.5758	0.7600	0.6552
		Full	0.5778	0.6250	0.6000	0.6122
	TwoLocal	1-pair mean	0.6926±0.0091	0.6914±0.0042	0.8067±0.0163	0.7446±0.0093
		2-pair mean	0.6489±0.0646	0.6488±0.0509	0.8080±0.0549	0.7192±0.0492
		3-pair mean	0.6556±0.0517	0.6527±0.0448	0.8200±0.0440	0.7261±0.0377
		4-pair mean	0.6163±0.0547	0.6195±0.0464	0.8240±0.0448	0.7055±0.0306
		5-pair mean	0.5778±0.0507	0.5855±0.0414	0.8533±0.0327	0.6928±0.0181
		6-pair mean	0.6444	0.6364	0.8400	0.7241
	TwoLocal	Best: (0,2)(0,3)	0.7556	0.7333	0.8800	0.8000
Blood	Classical: NonKernel	Random Forest	0.6222	0.6190	0.5909	0.6047
		Gradient Boosting	0.5778	0.5652	0.5909	0.5778
	Classical: Kernel	Linear SVM	0.6444	0.6071	0.7727	0.6800
		Polynomial SVM	0.6000	0.5833	0.6363	0.6087
		RBF SVM	0.6667	0.6667	0.6363	0.6512
	Pauli Z	Pauli Z	0.6667	0.6667	0.6364	0.6512
	Pauli ZZ	Linear	0.6000	0.6111	0.5000	0.5500
		Circular	0.5556	0.5455	0.5455	0.5455
		Full	0.6222	0.6087	0.6364	0.6222
	TwoLocal	1-pair mean	0.6667±0.0243	0.6659±0.0174	0.6364±0.0498	0.6504±0.0344
		2-pair mean	0.6578±0.0184	0.6597±0.0133	0.6182±0.0376	0.6380±0.0261
		3-pair mean	0.6633±0.0166	0.6639±0.0119	0.6295±0.0339	0.6461±0.0235
		4-pair mean	0.6667±0.0119	0.6665±0.0085	0.6364±0.0243	0.6510±0.0168
		5-pair mean	0.6630±0.0091	0.6639±0.0068	0.6288±0.0186	0.6458±0.0131
		6-pair mean	0.6667	0.6667	0.6364	0.6512
	TwoLocal	Best: (1,2)	0.6889	0.6818	0.6818	0.6818
Banknote	Classical: NonKernel	Random Forest	0.9111	0.9091	0.9091	0.9091
		Gradient Boosting	0.9111	0.9091	0.9091	0.9091
	Classical: Kernel	Linear SVM	0.9556	0.9167	1.0000	0.9565
		Polynomial SVM	0.9556	0.9167	1.0000	0.9565
		RBF SVM	0.9778	0.9561	1.0000	0.9778

Table 4 cont.

Dataset	Family	Model	Accuracy	Precision	Recall	F1
	Pauli Z	Pauli Z	0.9778	0.9565	1.0000	0.9778
	Pauli ZZ	Linear	0.6889	0.6538	0.7727	0.7083
		Circular	0.5778	0.5556	0.6818	0.6122
		Full	0.5111	0.5000	0.7273	0.5926
	TwoLocal	1-pair mean	0.9704±0.0181	0.9502±0.0311	0.9924±0.0186	0.9705±0.0180
		2-pair mean	0.9659±0.0142	0.9431±0.0250	0.9909±0.0188	0.9661±0.0141
		3-pair mean	0.9656±0.0134	0.9402±0.0201	0.9932±0.0167	0.9658±0.0133
		4-pair mean	0.9704±0.0108	0.9458±0.0182	0.9970±0.0117	0.9706±0.0106
		5-pair mean	0.9741±0.0091	0.9499±0.0163	1.0000±0.0000	0.9742±0.0087
		6-pair mean	0.9778	0.9565	1.0000	0.9778
	TwoLocal	Best: (0,1)	1.0000	1.0000	1.0000	1.0000

The results demonstrate that no single feature-map configuration consistently achieves the highest classification performance across all datasets. On Adhoc3_150, Random Forest achieves the highest accuracy at 0.8222, exceeding all evaluated quantum configurations. For Adhoc4_150, Pauli Z and the best-performing TwoLocal topology both achieve an accuracy of 0.7556. On Blood, the best TwoLocal topology reaches 0.6889, compared with 0.6667 for both RBF SVM and Pauli Z. On Banknote, the best TwoLocal configuration achieves perfect classification with an accuracy of 1.0000, while RBF SVM and Pauli Z both achieve 0.9778. These results indicate that the relative performance of quantum and classical approaches varies across datasets rather than following a consistent hierarchy.

The standard Pauli ZZ configurations do not provide a consistent performance improvement over the unentangled Pauli Z feature map. Across all four datasets, the linear, circular, and full Pauli ZZ configurations do not exceed the accuracy of Pauli Z. On Adhoc3_150, the linear topology obtains an accuracy of 0.4000, while the circular and full topologies both reach 0.6222 compared with 0.7778 for Pauli Z. On Adhoc4_150, the corresponding accuracies are 0.5556, 0.5556, and 0.5778 for the linear, circular, and full topologies, respectively, compared with 0.7556 for Pauli Z. On Blood, the three Pauli ZZ configurations obtain 0.6000, 0.5556, and 0.6222, respectively, compared with 0.6667 for Pauli Z. A similar pattern is observed on Banknote, where the linear, circular, and full configurations achieve 0.6889, 0.5778, and 0.5111, respectively, compared with 0.9778 for Pauli Z. Thus, the use of a predefined entanglement topology does not by itself guarantee improved classification performance.

The additional evaluation metrics provide a consistent picture of the classification results. Because the datasets were constructed or sampled with balanced class sizes, accuracy provides an appropriate primary metric for the comparative analysis, while precision, recall, and F1-score provide complementary information. Across the reported configurations, the rankings are largely consistent across these measures, and the F1-score differs from accuracy by less than 0.03 in nearly all conditions. Accordingly, accuracy is used as the primary performance indicator in the subsequent topology-level analysis.

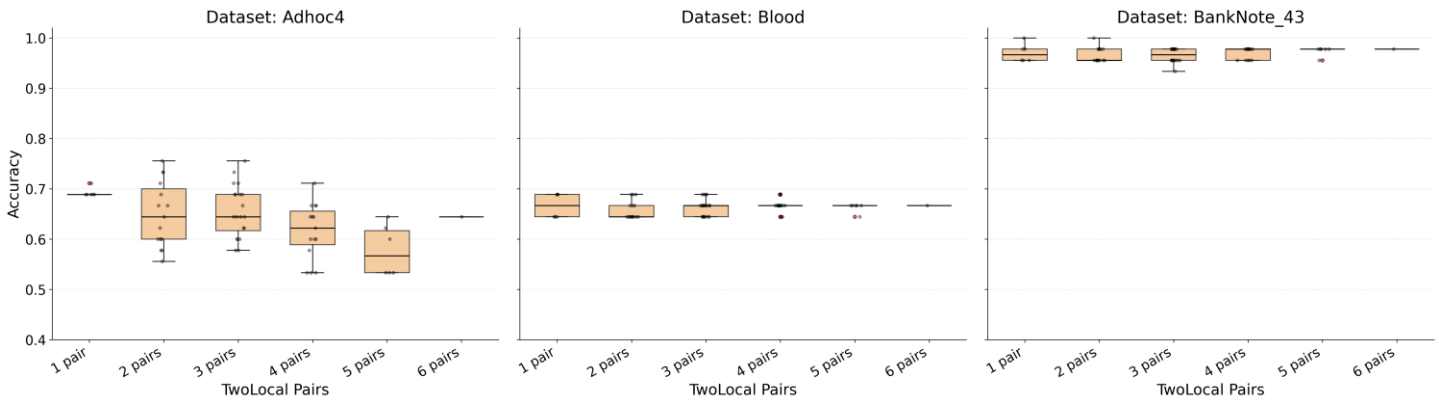

Figure 7. Accuracy Distribution Among Various Entanglement Schemes Grouped by The Number of Pairs on 4-feature Datasets

Beyond the comparison among feature-map families, the relationship between entanglement density and TwoLocal performance is examined in Figure 7. The results do not show a monotonic increase in accuracy as the number of entangling pairs increases. For Adhoc4_150, the mean accuracy decreases from 0.6926 for one pair to 0.5778 for five pairs before increasing to 0.6444 for the fully connected six-pair topology. Blood exhibits a comparatively flat pattern, with mean accuracy ranging from 0.6578 to 0.6667 across the pair-count groups. Banknote is similarly stable, with mean accuracy ranging from 0.9656 to 0.9778. These results indicate that entanglement density alone is insufficient to predict TwoLocal classification performance.

The identity of the individual topology also contributes to the observed variation within the pair-count groups. On Adhoc4_150, the highest accuracy of 0.7556 is achieved by two TwoLocal topologies belonging to different pair-count groups. The topology (0,2),(0,3) contains two entangling pairs, whereas (0,1),(0,2),(0,3) contains three pairs. Despite achieving the same maximum accuracy, their respective pair-count group means are only 0.6489 and 0.6556. The two-pair topology (0,2),(0,3) also achieves the highest F1-score and is therefore included in Figure 8. On Blood, the maximum accuracy of 0.6889 is shared by 12 TwoLocal topologies spanning one to four entangling pairs. Their compositions are reported in Table 5. The distribution of these high-performing configurations across several pair counts is consistent with the relatively flat accuracy means observed in Figure 7 and indicates that no single pair-count level clearly dominates on this dataset.

Table 4. The Composition of The 12 Quantum Feature Map Topologies on Blood Dataset achieving the highest value of both accuracy and F1-score

1 pair	2 pairs	3 pairs	4 pairs
((1,2))	((1,2), (1,3))	((0,1), (0,3), (2,3))	((0,2), (0,3), (1,2), (2,3))
((1,3))	((1,2), (2,3))	((0,2), (0,3), (1,2))	((0,2), (1,2), (1,3), (2,3))
((2,3))	((1,3), (2,3))	((0,2), (0,3), (1,3))	
		((1,2), (1,3), (2,3))	

On Banknote, two TwoLocal topologies achieve perfect performance, with accuracy, precision, recall, and F1-score all equal to 1.0000. These are the one-pair topology (0,1) and its four-qubit superset (0,1),(2,3), both shown in Figure 8. The additional entangling pair therefore does not change the classification performance in this case. This provides another example in which increasing the number of entangling pairs does not necessarily produce either an improvement or a degradation in performance.

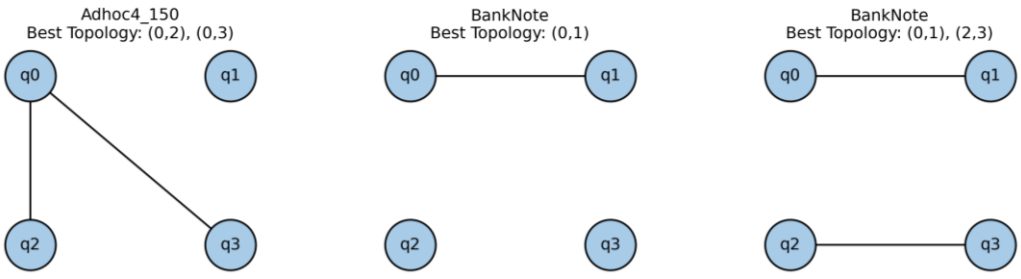

Figure 8. TwoLocal Feature Maps on Adhoc4_150 and Banknote achieving the highest value of both accuracy and F1-score

Taken together, the results show that the number of entangling pairs and the use of standard predefined topologies are insufficient to explain the performance of TwoLocal feature maps. Adhoc4_150 exhibits substantial variation across topology configurations, while Blood and Banknote show considerably more stable performance at the aggregate pair-count level. Nevertheless, the best-performing individual topology can differ substantially from the mean performance of its corresponding pair-count group, as observed on Adhoc4_150. Conversely, multiple topologies can achieve the same maximum performance, as observed on Blood and Banknote. These observations motivate the edge- and vertex-level sensitivity

analysis in Section 4.2, where the structural contribution of individual entanglement elements is examined directly.

Finally, the comparison with classical baselines places the quantum results in context. The strongest quantum configurations do not consistently outperform the strongest classical models: Random Forest remains the best-performing model on Adhoc3_150, whereas the best TwoLocal configurations achieve the highest accuracy on Blood and Banknote. Even in these cases, the observed improvements should not be interpreted as evidence of a general quantum advantage, particularly given the limited dataset sizes and the noiseless statevector simulation setting. Moreover, statevector simulation requires representation of a quantum state with dimension 2^n, resulting in exponential growth in simulation cost with the number of qubits. The observed dataset-specific accuracy improvements therefore do not, under the present experimental setting, establish that quantum kernel methods offset their associated computational overhead.

4.2. Factorial Linear Models for Entanglement Element Sensitivity Analysis

The variation observed across individual TwoLocal topologies motivates a more granular analysis of the structural elements that constitute each topology. The exhaustive enumeration provides a complete set of topology–accuracy observations for the four-qubit feature map, allowing the effect of individual entanglement elements to be examined using factorial linear models. Two complementary models are considered: an edge-based model that evaluates specific qubit-pair connections and a vertex-degree model that evaluates the connectivity density of individual qubits.

4.2.1. Edge Sensitivity Analysis

An Ordinary Least Squares (OLS) model was constructed to quantify the association between individual entanglement edges and classification accuracy. For the four-qubit TwoLocal feature map, there are six possible qubit-pair connections and therefore $2^6 - 1 = 63$ non-empty entanglement topologies. The accuracy obtained from each topology is used as the response variable, while each possible qubit pair is represented by a binary factor indicating whether the corresponding edge is present. The model is defined as:

$$\text{accuracy}_i = \beta_0 + \sum_e \beta_e \cdot x_{i,e} + \epsilon_i, \qquad \text{for } i = 0, 1, \dots, T-1 \tag{4}$$

where $x_{i,e} \in \{+1, -1\}$ denotes the presence or absence of edge e in topology i. The number of evaluated non-empty topologies is $T = 2^{(n^2-n)/2} - 1$, where n denotes the number of qubits. The residual term ϵ_i represents variation in accuracy not captured by the additive edge terms. The model then aims to find the best fitted value of coefficients (β_e) and intercepts ($\beta 0$) relative to the accuracy data. One distinct OLS model is fitted per dataset to map their separate performance response surfaces independently.

Table 5. Factorial Linear Model Coefficients for Qubit-Pair Sensitivity (Edge Sensitivity Analysis)

Qubit Pair	Adhoc4 Dataset ($\beta_0 = 0.6416$, $R^2 = 0.496$)				Blood Dataset ($\beta_0 = 0.6631$, $R^2 = 0.318$)				Banknote Dataset ($\beta_0 = 0.9682$, $R^2 = 0.556$)			
	β_e	SE	t	p-value	β_e	SE	t	p-value	β_e	SE	t	p-value
q1q3	-0.0048	0.0056	-0.8539	0.3968	0.0022	0.0018	1.2459	0.2180	-0.0043	0.0012	-3.7129	0.0005
q0q3	0.0001	0.0056	0.0152	0.9879	-0.0006	0.0018	-0.3322	0.7410	-0.0015	0.0012	-1.3080	0.1962
q0q1	-0.0395	0.0056	-7.0618	0.0000	-0.0048	0.0018	-2.6994	0.0092	0.0040	0.0012	3.5019	0.0009
q0q2	-0.0062	0.0056	-1.1022	0.2751	-0.0027	0.0018	-1.5158	0.1352	0.0020	0.0012	1.6982	0.0950
q1q2	-0.0117	0.0056	-2.0954	0.0407	0.0036	0.0018	2.0349	0.0466	-0.0022	0.0012	-1.9092	0.0614
q2q3	-0.0020	0.0056	-0.3572	0.7223	0.0057	0.0018	3.2185	0.0021	0.0068	0.0012	5.9069	0.0000

Under the -1/+1 effect coding, each coefficient β_e represents the estimated effect associated with the corresponding entanglement edge after accounting for the other additive edge terms in the model. Standard errors, t-statistics, and p-values are reported to characterize the magnitude and uncertainty of each estimated effect. Because the observations comprise the complete set of evaluated topologies rather than a random sample from a larger

population, the p-values are interpreted as descriptive indicators of the relative strength of the estimated effects rather than as conventional population-level sampling inference. The estimated coefficients for the three four-feature datasets are summarized in Table 6.

Furthermore, Figure 9 illustrates the estimated coefficients (β_e) for each qubit-pair edge, plotted with their 95% confidence intervals ($\beta_e \pm 1.96 \times$ SE), for the Adhoc4, Blood, and Banknote datasets. Each point marker denotes the point estimate of an edge's effect on classification accuracy, and the horizontal whiskers denote the confidence interval. An edge is labeled green ("Yes") if its two-tailed p-value falls below 0.05, and red ("No") otherwise. Equivalently, and as shown directly in the plot, a green interval lies entirely to one side of zero: either entirely negative or entirely positive. This indicates that zero is excluded from the 95% CI and the edge's effect is distinguishable from no effect at the chosen confidence level. A red interval, by contrast, straddles zero, indicating that the data cannot rule out a null effect for that edge at 95% confidence.

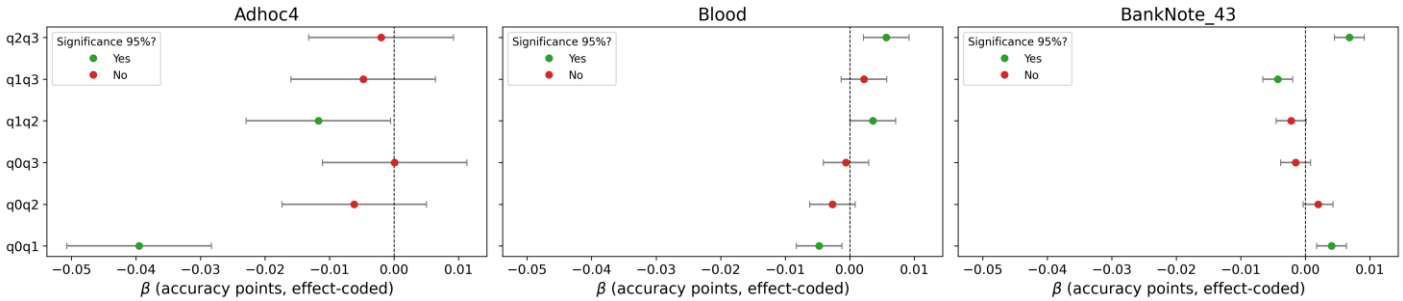

Figure 9. Forest Plot of Estimated Edge Effect Sizes (β_e) on Classification Accuracy with 95% Confidence Intervals: (left) Adhoc4_150, (center) Blood, and (right) Banknote Datasets

The edge-based linear models reveal that both the strength and the direction of entanglement's effect on accuracy are dataset-specific rather than fixed. First, model fit varies considerably across datasets: Banknote achieves the highest R^2 (0.556), followed by Adhoc4_150 (0.496), with Blood the lowest (0.318). Structural edge effects are therefore most linearly coherent on Banknote and least so on Blood, the reverse of what the aggregate accuracy spread alone would suggest (Figure 7). Second, the sign and identity of significant edges differ by dataset. On Adhoc4_150, two edges show a statistically significant (meaning that their p values are smaller than 0.05) negative effect: q0q1 and q1q2, displaying wide margins of strongest effect observed in this analysis, whereas no other edge shows a significant positive effect. On Blood, one edge is significantly negative (q0q1) while two are significantly positive (q1q2 and q2q3). On Banknote, three edges reach significance, split in both directions: q1q3 is negative, while q0q1 and q2q3 are positive. Notably, the edge q0q1 is significant in all three datasets but changes sign (strongly negative on Adhoc4_150, weakly negative on Blood, positive on Banknote), demonstrating directly that no single edge has a fixed, dataset-independent effect on classification accuracy; its contribution depends on the specific feature map and data distribution in which it is embedded.

4.2.2. Vertex-Degree Sensitivity Analysis

The edge-based model identifies the contribution associated with specific qubit pairs. A complementary analysis considers whether the overall connectivity of an individual qubit is associated with classification accuracy, regardless of the identity of its connected partners. For topology i and qubit $v \in \{0, 1, 2, 3\}$, the vertex degree $d_{i,v} \in \{0, 1, 2, 3\}$, denotes the number of entanglement edges incident to qubit v. The vertex-degree model is defined as:

$$\text{accuracy}_i = \gamma_0 + \sum_{v=0}^{3} \gamma_v \cdot (d_{i,v} - \bar{d}) + \epsilon_i, \qquad \text{for } i = 0, 1, \ldots, T-1. \tag{5}$$

Centering the degree variable around its mean, $\bar{d}$, allows the coefficients γ_v to represent the estimated change in accuracy associated with increasing the connectivity of qubit v. The resulting coefficient estimates, together with their standard errors, t-statistics, p-values, and model fit, are reported in Table 7 and visualized in Figure 10.

Table 6. Factorial Linear Model Coefficients for Per-Qubit Connectivity (Vertex-Degree Sensitivity Analysis)

Qubit	Adhoc4 Dataset ($\gamma_0 = 0.6406$, $R^2 = 0.407$)				Blood Dataset ($\gamma_0 = 0.6631$, $R^2 = 0.306$)				Banknote Dataset ($\gamma_0 = 0.9683$, $R^2 = 0.164$)			
	γ_v	SE	t	p-value	γ_v	SE	t	p-value	γ_v	SE	t	p-value
q0	-0.0242	0.0077	-3.1577	0.0025	-0.0091	0.0022	-4.0755	0.0001	0.0029	0.0020	1.4413	0.1549
q1	-0.0346	0.0077	-4.5158	0.0000	-0.0001	0.0022	-0.0543	0.9569	-0.0041	0.0020	-2.0252	0.0475
q2	0.0015	0.0077	0.1922	0.8483	0.0054	0.0022	2.4203	0.0187	0.0050	0.0020	2.4813	0.0160
q3	0.0147	0.0077	1.9124	0.0608	0.0061	0.0022	2.7297	0.0084	-0.0006	0.0020	-0.2919	0.7714

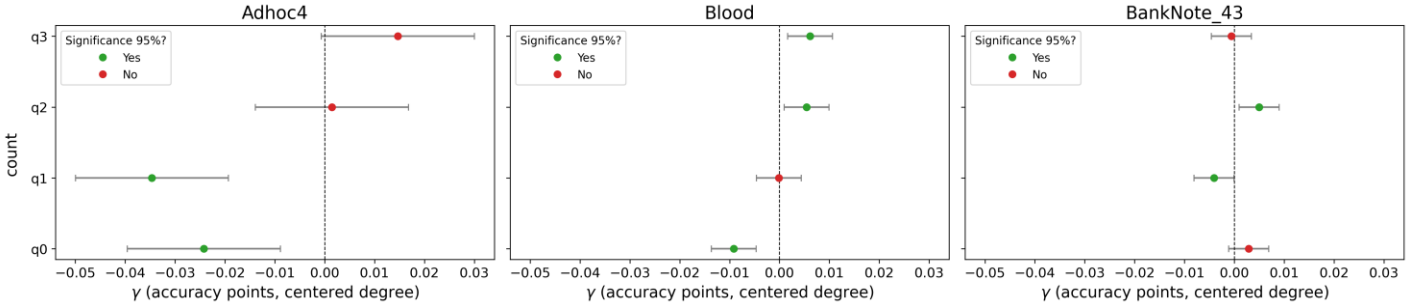

Figure 10. Forest Plot of Estimated Vertex Effect Sizes (γ_v) on Classification Accuracy with 95% Confidence Intervals: (left) Adhoc4_150, (center) Blood, and (right) Banknote Datasets

The vertex-degree models explain less variation than the corresponding edge-based models for all three datasets. The resulting R^2 values are 0.407 for Adhoc4_150, 0.306 for Blood, and 0.164 for Banknote, compared with 0.496, 0.318, and 0.556, respectively, for the edge-based models. The difference is particularly pronounced for Banknote, where the edge-based model explains substantially more variation than the vertex-degree model. This indicates that, for this dataset, the identity of the qubit pairings contains considerably more information about accuracy than the overall connectivity degree of an individual qubit.

The estimated vertex effects also vary across datasets. On Adhoc4_150, q0 and q1 exhibit significant negative effects, with coefficients of -0.0242 and -0.0346, respectively, whereas q2 and q3 do not reach statistical significance. On Blood, q0 has a significant negative effect β=-0.0091, while q2 and q3 have significant positive effects β =0.0054 and 0.0061, respectively). On Banknote, q1 has a significant negative effect β=-0.0041 and q2 has a significant positive effect β =0.0050, while q0 and q3 are not significant.

The comparison between the edge- and vertex-degree analyses further shows that these models capture distinct structural properties. For example, on Banknote, q1 has a significant negative vertex-degree effect, whereas the q0q1 edge incident to the same qubit has a significant positive effect in the edge-based model. Thus, greater connectivity of q1 is associated with lower accuracy on average, while one specific connection involving q1 is associated with higher accuracy. This distinction demonstrates why qubit-level connectivity cannot be interpreted simply as a summary of individual edge effects.

4.2.3 Limitations and Opportunities of the Evaluative Framework

The factorial sensitivity analysis provides an interpretable representation of edge- and qubit-level effects, but two limitations constrain its current scope. First, exhaustive topology enumeration becomes increasingly difficult as the number of qubits increases. The number of non-empty entanglement topologies for an n-qubit feature map is $2^{\binom{n}{2}} - 1$, resulting in 7, 63, 1,023, and 32,767 possible topologies for 3, 4, 5, and 6 qubits, respectively. This combinatorial growth is compounded by the exponential state-space cost of statevector simulation. Consequently, the exhaustive procedure used in this study is primarily practical for low-qubit systems.

The factorial models themselves are not mathematically restricted to exhaustive enumeration. Given a set of topology–accuracy observations, the same formulation can be applied to randomly or systematically sampled topologies from a larger topology space or to results obtained from other datasets. However, the reliability and stability of coefficient estimates

under incomplete topology sampling have not been empirically established in this study. Validation against exhaustive ground truth at moderate qubit counts therefore remains an important direction for future work.

Second, both models assume an additive relationship between the structural predictors and classification accuracy. In the edge-based model, each edge coefficient represents an effect that does not explicitly depend on which other edges are simultaneously present. Likewise, the vertex-degree model assumes additive contributions from the connectivity degrees of individual qubits. Potential edge–edge interactions are therefore not represented explicitly. For example, two edges may have a combined effect that differs from the sum of their individual effects, or the effect of one edge may depend on the presence of an adjacent edge. Such higher-order dependencies are absorbed into the residual term and may partly explain the moderate R^2 values observed in the models. These limitations define two principal opportunities for extending the framework: evaluating the stability of attribution under incomplete topology sampling and incorporating interaction-aware or nonlinear models to capture dependencies among entanglement elements. Both extensions remain beyond the scope of the present study.

5. Conclusions

This study investigated how entanglement topology influences quantum kernel SVM classification by exhaustively evaluating the feasible entanglement configurations of a TwoLocal feature map and comparing them with classical and standard quantum feature maps across two synthetic and two real-world datasets. The results show that neither entanglement density nor a predefined topology consistently determines classification performance. The strongest configuration was dataset dependent, with Random Forest performing best on Adhoc3_150, Pauli Z tying with the best TwoLocal configuration on Adhoc4_150, and specific non-standard TwoLocal topologies achieving the highest accuracy on Blood and Banknote. In contrast, the standard linear, circular, and full Pauli ZZ configurations did not outperform Pauli Z on any dataset. Thus, the classification effect of entanglement is better understood in terms of topology-specific structure than entanglement density alone.

The central methodological contribution is the factorial sensitivity framework enabled by exhaustive topology evaluation. By decomposing topology-level results into edge- and vertex-degree effects, the approach provides a more granular characterization of how individual qubit connections and connectivity patterns are associated with classification accuracy. The analysis revealed dataset-dependent effects, including a significant q0q1 edge whose direction changed across datasets. The comparison between edge- and vertex-degree models further showed that overall qubit connectivity does not necessarily capture the effect of specific pairings. These findings address the central limitation of conventional topology comparisons, which evaluate whole-circuit configurations without distinguishing the contributions of their constituent entanglement elements.

The observed quantum performance should nevertheless be interpreted within the scope of the experimental setting. Although selected TwoLocal configurations achieved the highest accuracy on Blood and Banknote, these dataset-specific results do not establish a general quantum advantage. The experiments used limited-size datasets and noiseless statevector simulation, while the computational cost of statevector simulation increases exponentially with the number of qubits. The primary contribution of the study is therefore the structural characterization of entanglement effects rather than a claim of quantum superiority over classical methods. The factorial formulation is not intrinsically limited to exhaustive enumeration or to the datasets examined here. It can, in principle, be applied to a selected collection of topology–accuracy observations, providing a potential route toward larger topology spaces where exhaustive evaluation is impractical. However, this transferability is a property of the formulation rather than an empirically validated result of the present study. The specific coefficients and structural effects reported here should therefore be interpreted as results for the evaluated datasets and qubit scales.

Future work should validate the framework under larger and more diverse experimental settings, particularly through sampled-topology evaluation at higher qubit counts and experiments involving realistic noise or quantum hardware. Extending the analysis to joint variation of rotation blocks, entanglement blocks, and circuit depth would also clarify whether the observed structural effects persist across different feature-map architectures. Finally,

incorporating interaction terms or using the resulting sensitivity estimates to guide topology search could transform the current post-hoc analysis into a more targeted approach for automated quantum feature-map design.

Author Contributions: Conceptualization: NN, HS and YT.; Methodology: HS; Software: NN; Validation: HS, YT; Investigation: NN; Data curation: NN; Writing original draft preparation: NN, YT; Writing review and editing: NN, HS and YT; Visualization: NN, YT; Supervision: HS; Project administration: HS; Funding acquisition: HS. All authors have read and agreed to the published version of the manuscript.

Funding: This work was funded by PT Lancs Arche Consumma (MOU.003/CIT/XI/2022).

Code Availability: The code used in this study has been deposited in GitHub (https://github.com/QCRG-CRC/Quantum-Kernel-Entanglement-Analysis).

Acknowledgments: During the preparation of this article, the authors employed Claude and ChatGPT to enhance the readability by improving sentence structures and grammar checking. After using these services, the authors reviewed and edited the content as needed and take full responsibility for the publication's content.

Conflicts of Interest: The authors declare that they have no known competing financial or non-financial interests or personal relationships that could have appeared or influence the work reported in this paper.

References

[1] M. A. Nielsen and I. L. Chuang, Quantum Computation and Quantum Information, 10th Anniv. Cambridge, UK: Cambridge University Press, 2010.
[2] J. Preskill, "Quantum Computing in the NISQ Era and Beyond," Quantum, vol. 2, p. 79, 2018, doi: 10.22331/q-2018-08-06-79.
[3] M. Motta and J. E. Rice, "Emerging quantum computing algorithms for quantum chemistry," Wiley Interdiscip. Rev. Comput. Mol. Sci., vol. 12, no. 3, p. e1580, 2022, doi: https://doi.org/10.1017/CBO9780511976667.
[4] M. Imran, A. B. Altamimi, W. Khan, S. Hussain, M. Alsaffar, and others, "Quantum cryptography for future networks security: A systematic review," IEEE Access, vol. 12, pp. 180048–180078, 2024, doi: 10.1109/ACCESS.2024.3504815.
[5] M. Cerezo, G. Verdon, H.-Y. Huang, L. Cincio, and P. J. Coles, "Challenges and opportunities in quantum machine learning," Nat. Comput. Sci., vol. 2, no. 9, pp. 567–576, 2022, doi: 10.1038/s43588-022-00311-3.
[6] J. Chen and Y. Li, "Empowering complex-valued data classification with the variational quantum classifier," Front. Quantum Sci. Technol., vol. 3, 2024, doi: 10.3389/frqst.2024.1282730.
[7] H.-X. Yin, Z.-Y. Hu, H.-H. Zeng, J.-B. Guan, and J. Wang, "Application of quantum machine learning using variational quantum classifier in accelerator physics," 2025, doi: 10.1007/s41365-026-02016-y.
[8] M.-G. Zhou, Z.-P. Liu, H.-L. Yin, C.-L. Li, T.-K. Xu, and Z.-B. Chen, "Quantum neural network for quantum neural computing," Research, vol. 6, p. 134, 2023, doi: 10.34133/research.0134.
[9] L.-H. Gong, J.-J. Pei, T.-F. Zhang, and N.-R. Zhou, "Quantum convolutional neural network based on variational quantum circuits," Opt. Commun., vol. 550, p. 129993, 2024, doi: 10.1016/j.optcom.2023.129993.
[10] A. S. Bhatia and D. E. B. Neira, "Federated learning with tensor networks: a quantum AI framework for healthcare," Mach. Learn. Sci. Technol., vol. 5, no. 4, p. 45035, 2024, doi: 10.1088/2632-2153/ad8c11.
[11] V. Havlíček and others, "Supervised learning with quantum-enhanced feature spaces," Nature, vol. 567, no. 7747, pp. 209–212, 2019, doi: 10.1038/s41586-019-0980-2.
[12] A. Javadi-Abhari and others, "Quantum computing with Qiskit," 2024. doi: 10.48550/arXiv.2405.08810.
[13] M. E. Sahin and others, "Qiskit machine learning: an open-source library for quantum machine learning tasks at scale on quantum hardware and classical simulators," 2025. doi: 10.48550/arXiv.2505.17756.
[14] S. Sim, P. D. Johnson, and A. Aspuru-Guzik, "Expressibility and Entangling Capability of Parameterized Quantum Circuits for Hybrid Quantum-Classical Algorithms," Adv. Quantum Technol., vol. 2, no. 12, p. 1900070, 2019, doi: 10.1002/qute.201900070.
[15] D. Valkenborg, A.-J. Rousseau, M. Geubbelmans, and T. Burzykowski, "Support vector machines," Am. J. Orthod. Dentofac. Orthop., vol. 164, no. 5, pp. 754–757, 2023, doi: 10.1016/j.ajodo.2023.08.003.
[16] M. N. Murty and R. Raghava, "Kernel-based SVM," in Support Vector Machines and Perceptrons: Learning, Optimization, Classification, and Application to Social Networks, Springer, 2016, pp. 57–67. doi: 10.1007/978-3-319-41063-0_5.
[17] J. Wang, Q. Chen, and Y. Chen, "RBF kernel based support vector machine with universal approximation and its application," in International Symposium on Neural Networks, 2004, pp. 512–517. doi: 10.1007/978-3-540-28647-9_85.
[18] M. Schuld and N. Killoran, "Quantum machine learning in feature Hilbert spaces," Phys. Rev. Lett., vol. 122, no. 4, p. 40504, 2019, doi: 10.1103/PhysRevLett.122.040504.
[19] D. Sharma, P. Singh, and A. Kumar, "The role of entanglement for enhancing the efficiency of quantum kernels towards classification," Phys. A Stat. Mech. its Appl., 2023, doi: 10.1016/j.physa.2023.128938.

[20] C. Ding, S. Wang, Y. Wang, and W. Gao, "Quantum machine learning for multiclass classification beyond kernel methods," Phys. Rev. A, vol. 111, p. 62410, 2025, doi: 10.1103/PhysRevA.111.062410.
[21] A. Babu, S. G. Ghatnekar, A. Saxena, and D. Mandal, "Entanglement-enabled quantum kernels for enhanced feature mapping," APL Quantum, vol. 2, no. 1, p. 16116, 2025, doi: 10.1063/5.0240894.
[22] I.-C. Dinut, R.-C. Constantinescu, and B. Alexandrescu, "Comparative Analysis and Noise Robustness Study of Quantum Kernel Methods and Variational Quantum Classifiers for Financial Fraud Detection," Electronics, vol. 15, no. 11, p. 2489, 2026, doi: 10.3390/electronics15112489.
[23] F. El Ayachi and M. El Baz, "Enhancing quantum support vector machines using multipartite entanglement," Phys. Lett. A, vol. 551, p. 130666, 2025, doi: 10.1016/j.physleta.2025.130666.
[24] Y. Tjandra and H. S. Sugiarto, "Metaheuristic optimization scheme for quantum kernel classifiers using entanglement-directed graphs," ETRI J., vol. 46, no. 5, pp. 793–805, 2024, doi: 10.4218/etrij.2024-0144.
[25] Y. Tjandra and H. S. Sugiarto, "An Evolutionary Algorithm Design for Pauli-based Quantum Kernel Classification," in Proceedings of the International Workshop on Quantum Data Science and Management (QDSM'23), in CEUR Workshop Proceedings, vol. 3462. 2023. [Online]. Available: https://ceur-ws.org/Vol-3462/QDSM3.pdf
[26] J. Bowles, S. Ahmed, and M. Schuld, "Better than classical? The subtle art of benchmarking quantum machine learning models," Mar. 2024. doi: 10.48550/arXiv.2403.07059.
[27] J. Schnabel and M. Roth, "Quantum kernel methods under scrutiny: a benchmarking study," Quantum Mach. Intell., vol. 7, no. 1, Jun. 2025, doi: 10.1007/s42484-025-00273-5.
[28] R. Heese, T. Gerlach, S. Mücke, S. Müller, M. Jakobs, and N. Piatkowski, "Explaining quantum circuits with Shapley values: towards explainable quantum machine learning," Quantum Mach. Intell., vol. 7, no. 1, Jun. 2025, doi: 10.1007/s42484-025-00254-8.
[29] Y. Jiang and M. Otten, "Benchmarking Quantum Kernels Across Diverse and Complex Data," 2025.
[30] I.-C. Yeh, K.-J. Yang, and T.-M. Ting, "Knowledge discovery on RFM model using Bernoulli sequence," Expert Syst. Appl., vol. 36, no. 3, pp. 5866–5871, 2009, doi: 10.1016/j.eswa.2008.07.018.
[31] V. Lohweg, "Banknote Authentication," 2012. doi: 10.24432/C55P57.
[32] A. F. A. H. Alnuaimi and T. H. K. Albaldawi, "An overview of machine learning classification techniques," in BIO Web of Conferences, 2024, p. 133. doi: 10.1051/bioconf/20249700133.
[33] M. Schuld and N. Killoran, "Is quantum advantage the right goal for quantum machine learning?," PRX Quantum, vol. 3, no. 3, p. 30101, 2022, doi: 10.1103/PRXQuantum.3.030101.
[34] F. Pedregosa and others, "Scikit-learn: Machine learning in Python," J. Mach. Learn. Res., vol. 12, pp. 2825–2830, 2011.